Available online at www.sciencedirect.com
SCIENCE DIRECT®
Comput. Methods Appl. Mech. Engrg. 192 (2003) 2355–2375
Computer methods in applied mechanics and engineering
www.elsevier.com/locate/cma

Coupling of the mesh-free finite cloud method with the boundary element method: a collocation approach

Gang Li [a], Glaucio H. Paulino [b,*], N.R. Aluru [c]

[a] *Beckman Institute and Department of Mechanical and Industrial Engineering, University of Illinois at Urbana-Champaign, Urbana, IL 61801, USA*

[b] *Department of Civil and Environmental Engineering, Newmark Laboratory, University of Illinois at Urbana-Champaign, 205 North Mathews Avenue, Urbana, IL 61801-2352, USA*

[c] *Beckman Institute and Department of General Engineering, University of Illinois at Urbana-Champaign, Urbana, IL 61801, USA*

Received 8 July 2002; received in revised form 15 January 2003

Abstract

Meshless and mesh-based methods are among the tools frequently applied in the numerical treatment of partial differential equations (PDEs). This paper presents a coupling of the meshless finite cloud method (FCM) and the standard (mesh-based) boundary element method (BEM), which is motivated by the complementary properties of both methods. While the BEM is appropriate for solving linear PDEs with constant coefficients in bounded or unbounded domains, the FCM is appropriate for either homogeneous, inhomogeneous or even nonlinear problems in bounded domains. Both techniques (FCM and BEM) use a collocation procedure in the numerical approximation. No mesh is required in the FCM subdomain and its nodal point distribution is completely independent of the BEM subdomain. The coupling approach is demonstrated for linear elasticity problems. Because both FCM and BEM employ traction–displacement relations, no transformations between forces and tractions (typical of BEM and finite element coupling) are needed. Several numerical examples are given to demonstrate the proposed approach.

Keywords: Boundary element method; Finite cloud method; Meshless methods; Coupling techniques; Collocation

1. Introduction

Recently, domain-based meshless techniques [1] have emerged as a new viable alternative to do computational analysis of various physical problems. Common features of these methods are: (1) particles or points instead of elements are used to discretize the physical domain; (2) interpolations are constructed without requiring connectivity information among the particles; and (3) collocation or Galerkin (either local or global) methods are used for discretization of the governing equations. Meshless methods provide great flexibility to numerical analysis of many complicated problems.

* Corresponding author. Tel.: +1-217-337-5338/333-3817; fax: +1-217-265-8041.
E-mail address: paulino@uiuc.edu (G.H. Paulino).

0045-7825/03/$ - see front matter © 2003 Elsevier Science B.V. All rights reserved.
doi:10.1016/S0045-7825(03)00258-5

In this paper, a coupling approach to combine a meshless method, namely the finite cloud method (FCM) [2], with the standard boundary element method (BEM) is proposed and demonstrated for elasticity problems. The FCM uses a fixed kernel approximation for construction of meshless interpolation functions, and a collocation method for discretizing the governing partial differential equations (PDEs). The BEM utilizes boundary integral equations and fundamental solutions (or Green's functions) to compute the unknown displacements and tractions. The final linear system obtained from the FCM is then assembled with the final linear system obtained from the BEM. There are several advantages of the proposed approach over the conventional coupling between the BEM and the finite element method (FEM), as listed below.

- FCM does not require a mesh or background cells for integration—it is a true meshless method. Only points need to be sprinkled over the domain.
- FCM and BEM share the same set of nodes at common boundaries. There is no interpolation needed to transfer numerical quantities between the two domains.
- Point refinement in the FCM domain and mesh refinement in BEM domain are independent. Thus the coupling scheme is not restricted by the order of boundary elements employed.
- In elasticity applications, both BEM and FCM are inherently based on traction–displacement formulations. Thus the coupling of the two methods does not require any transformation between forces and tractions.

The remainder of this paper is organized as follows. A brief literature review involving related work on coupling of numerical methods is given in Section 2. The FCM for two-dimensional (2-D) elastostatics is presented in Section 3, the standard BEM for 2-D elastostatics is summarized in Section 4, the FCM/BEM coupling approach is introduced in Section 5, and numerical results are given in Section 6. Finally conclusions are inferred and potential extensions of this work are discussed in Section 7.

2. Related work

The coupling of different numerical methods has attracted attention of the engineering community because of the potential advantages associated with each of the methods being considered in the coupling approach. For instance, several researchers have coupled two domain-based methods, the FEM and a meshless method such as the element-free Galerkin (EFG) method or the reproducing kernel particle method (RKPM) [3–7], with various goals and using different formulations. Belytschko et al. [3] and Krongauz and Belytschko [4] have coupled the FEM and the EFG as a means to enforce the essential boundary conditions in meshless approximations. The technique is based on a string of finite elements along the essential boundaries. The shape functions from these edge finite elements are then combined with the shape functions of the meshless method so that the essential boundary conditions can be enforced. With similar objectives, Hegen [5] has presented a different EFG/FEM coupling approach where the FEM domain and the meshless region are connected by means of Lagrange multipliers. Huerta and Fernández-Méndez [6] have developed a general formulation using mixed interpolations for EFG/FEM coupling and for enrichment of the finite element mesh with particles. Liu et al. [7] have presented a scheme to enrich the finite element approximation with the RKPM.

Boundary-based methods may be coupled with domain-based methods to take advantage of the best properties of both methods. In the literature, most efforts have concentrated on coupling the BEM with the FEM, and several approaches have been proposed to treat these mesh-based methods. *Differently from previous approaches, the contribution of the present work is on coupling the mesh-based BEM with the meshless FCM.* However, due to the advances and relevance of FEM/BEM coupling, a brief discussion on this subject matter is in order.

The FEM is successful in dealing with inhomogeneities and nonlinearities, while the BEM may be more appropriate for unbounded problems such as infinite domain and exterior problems. In some applications, it is advantageous to combine the two methods [8] to achieve high-quality solutions [9–12]. In the last decade, the FEM/BEM coupling approaches have been applied to solve various problems in engineering, such as soil–structure interactions [13], fluid–structure interactions [14], contact problems [15], electromagnetics [16,17], elastodynamics [18,19], and medical problems [20]. There has also been a significant amount of work in the symmetric FEM/BEM coupling [14,17,21–24].

Consider, for instance, an application involving elastostatics. In general, there are three major FEM/BEM coupling approaches [9]: (1) using the finite element solution as the boundary conditions for the boundary element subdomain; (2) treating the boundary element subdomain as a finite element and embedding it into the finite element system—in this approach, the traction–displacement relations of BEM are transformed to FEM force–displacement relations; and (3) treating the finite element subdomain as an equivalent boundary element and embedding it to the boundary element system—in this approach, the force–displacement relations of FEM are transformed to BEM traction–displacement relations. Approaches (2) and (3) are commonly used in the literature [9–11]. However, the transformation between traction–displacement and force–displacement relations require extra matrix inversion and interpolation. Moreover, when FEM and BEM nodes do not coincide, additional interpolations are required. It is shown below that the present BEM/FCM coupling approach does not present any of these problems, which are typical of BEM/FEM coupling.

3. Finite cloud method for 2-D elastostatics

3.1. Governing equations

We will be primarily concerned with two-dimensional linear elastostatic analysis in this work. For small mechanical deformations, the linear theory of elasticity is used [25].

$$\nabla \cdot (\boldsymbol{\sigma}) + \mathbf{b} = 0 \quad \text{in } \Omega, \tag{1}$$

$$\mathbf{u} = \mathbf{g} \quad \text{on } \Gamma_g, \tag{2}$$

$$\boldsymbol{\sigma} \cdot \mathbf{n} = \mathbf{h} \quad \text{on } \Gamma_h, \tag{3}$$

where $\boldsymbol{\sigma}$ is the Cauchy stress tensor, $\mathbf{b}$ is the body force vector, $\mathbf{u}$ is the displacement vector, $\mathbf{g}$ is the prescribed displacement vector on the boundary portion Γ_g, $\mathbf{h}$ is the surface traction vector on the boundary portion Γ_h, $\mathbf{n}$ is the unit outward normal vector, and the dot denotes the inner product.

3.2. Relevant aspects of the FCM

The FCM uses a fixed kernel approximation [2,26] to construct the meshless interpolation functions and a point collocation technique [27] to discretize the governing partial differential equations (PDEs). In the following, we outline the steps used for the construction of interpolation functions (see [2] for more details). The domain is first represented by a set of points (or nodes), as shown in Fig. 1. Then, for each point, an interpolation function is generated by constructing a cloud about that node (also referred as a star node). A cloud is constructed by centering a kernel about the star point. The kernel is typically a cubic spline or a Gaussian function. The kernel is non-zero at the star point and at few other nodes that are in the vicinity of the star point. The shape of the cloud, which defines the nodes at which the kernel is non-zero, can be arbitrary. Typical shapes used in 2-D applications are circles and rectangles.

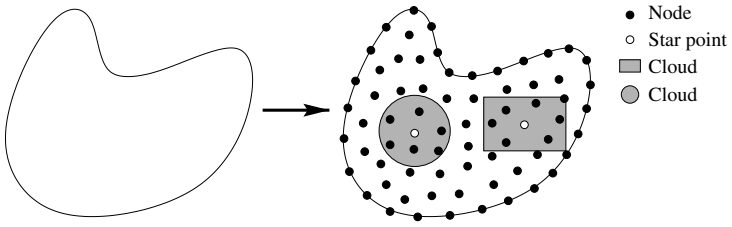

Fig. 1. The physical domain (left) is represented by a set of points (right), and clouds are constructed at each point. Also shown in the figure are a circular and a rectangular cloud.

In a meshless fixed kernel approach, an approximation $u^a(x,y)$ to an unknown $u(x,y)$ is given by

$$u^a(x,y) = \int_\Omega \mathscr{C}(x,y,x_k-s,y_k-t)\phi(x_k-s,y_k-t)u(s,t)\,\mathrm{d}s\,\mathrm{d}t, \tag{4}$$

where $\mathscr{C}(x,y,s,t)$ is the correction function which is given by

$$\mathscr{C}(x,y,x_k-s,y_k-t) = \mathbf{p}^T(x_k-s,y_k-t)\mathbf{c}(x,y), \tag{5}$$

ϕ is the kernel function centered at (x_k,y_k), which is usually taken as a cubic spline or a Gaussian function. In this paper, ϕ is taken as the following modified Gaussian function

$$\phi(x-x_I) = \frac{w(x-x_I)}{1-w(x-x_I)+\hat{\varepsilon}}, \tag{6}$$

where $\hat{\varepsilon}$ is a small number which is used to avoid the singularity of $\phi(x-x_I)$. In this paper, $\hat{\varepsilon}$ is chosen to be 10^{-5}. The expression $w(x-x_I)$ is a normalized Gaussian function given by

$$w(z) = \begin{cases} \dfrac{\mathrm{e}^{-(z/c)^2}-\mathrm{e}^{-(d_{mi}/c)^2}}{1-\mathrm{e}^{-(d_{mi}/c)^2}} & z \leqslant d_{mi}, \\ 0 & z > d_{mi}, \end{cases} \tag{7}$$

where d_{mi} is the support size of a cloud, c is the dilation parameter which is taken as $d_{mi}/2$. In 2-D, the kernel function is constructed as

$$\phi(x-x_I,y-y_I) = \phi(x-x_I)\phi(y-y_I). \tag{8}$$

The $1\times m$ vector $\mathbf{p}^T = \{p_1,p_2,\ldots,p_m\}$ contains the basis functions. In 2-D, a quadratic basis vector is given by

$$\mathbf{p}^T = [1, x_k-s, y_k-t, (x_k-s)^2, (x_k-s)(y_k-t), (y_k-t)^2] \quad m=6 \tag{9}$$

and $\mathbf{c}(x,y)$ is an $m\times 1$ vector of unknown correction function coefficients. The correction function coefficients are computed by enforcing the *consistency conditions*, i.e.,

$$\int_\Omega \mathbf{p}^T(x_k-s,y_k-t)\mathbf{c}(x,y)\phi(x_k-s,y_k-t)p_i(s,t)\,\mathrm{d}s\,\mathrm{d}t = p_i(x,y) \quad i=1,2,\ldots,m. \tag{10}$$

In discrete form, Eq. (10) can be rewritten as

$$\sum_{I=1}^{\mathrm{NP}} \mathbf{p}^T(x_k-x_I,y_k-y_I)\mathbf{c}(x,y)\phi(x_k-x_I,y_k-y_I)p_i(x_I,y_I)\Delta V_I = p_i(x,y) \quad i=1,2,\ldots,m, \tag{11}$$

where NP is the number of points in the domain, and ΔV_I is the nodal volume associated with node I (see [2] for a discussion on nodal volumes). Eq. (11) can be written in matrix form as

$$\mathbf{Mc}(x,y) = \mathbf{p}(x,y), \tag{12}$$

with

$$M_{ij} = \sum_{I=1}^{\mathrm{NP}} p_j(x_k - x_I, y_k - y_I)\phi(x_k - x_I, y_k - y_I)p_i(x_I, y_I)\Delta V_I \quad i,j = 1,2,\ldots,m. \tag{13}$$

From Eq. (12), the unknown correction function coefficients are computed as

$$\mathbf{c}(x,y) = \mathbf{M}^{-1}\mathbf{p}(x,y). \tag{14}$$

Substituting the correction function coefficients into Eq. (5) and employing a discrete approximation for Eq. (4), we obtain

$$u^a(x,y) = \sum_{I=1}^{\mathrm{NP}} N_I(x,y)\hat{\boldsymbol{u}}_I, \tag{15}$$

where $\hat{\boldsymbol{u}}_I$ is the nodal parameter for node I, and $N_I(x,y)$ is the fixed kernel meshless interpolation function defined as

$$N_I(x,y) = \mathbf{p}^T(x,y)\mathbf{M}^{-T}\mathbf{p}(x_k - x_I, y_k - y_I)\phi(x_k - x_I, y_k - y_I)\Delta V_I. \tag{16}$$

The derivatives of the unknown u are approximated by

$$\frac{\partial u^a(x,y)}{\partial x} = \sum_{I=1}^{\mathrm{NP}} \frac{\partial N_I(x,y)}{\partial x}\hat{\boldsymbol{u}}_I, \qquad \frac{\partial u^a(x,y)}{\partial y} = \sum_{I=1}^{\mathrm{NP}} \frac{\partial N_I(x,y)}{\partial y}\hat{\boldsymbol{u}}_I, \tag{17}$$

$$\frac{\partial^2 u^a(x,y)}{\partial x^2} = \sum_{I=1}^{\mathrm{NP}} \frac{\partial^2 N_I(x,y)}{\partial x^2}\hat{\boldsymbol{u}}_I, \qquad \frac{\partial^2 u^a(x,y)}{\partial y^2} = \sum_{I=1}^{\mathrm{NP}} \frac{\partial^2 N_I(x,y)}{\partial y^2}\hat{\boldsymbol{u}}_I, \tag{18}$$

$$\frac{\partial^2 u^a(x,y)}{\partial x \partial y} = \sum_{I=1}^{\mathrm{NP}} \frac{\partial^2 N_I(x,y)}{\partial x \partial y}\hat{\boldsymbol{u}}_I. \tag{19}$$

Fig. 2 shows the plots of a typical 2D fixed kernel interpolation function and its derivatives.

After the interpolation functions are constructed, the FCM uses a point collocation technique to discretize the governing equations. In point collocation, the governing equations are satisfied at every node which does not carry a boundary condition. For nodes with prescribed boundary conditions the approximate solution or the derivative of the approximate solution are set to the given displacement and traction boundary conditions, respectively. The point collocation approach gives rise to a linear system of equations, the solution of which provides the nodal parameters at nodes. Once the nodal parameters are computed, the unknown solution at each node can be computed from Eq. (15).

3.3. FCM for linear elasticity

For two-dimensional elasticity, there are two unknowns associated with each node in the domain, namely the displacements in the x and y directions. The governing equations given in Eq. (1), assuming zero body force, can be rewritten as the Navier–Cauchy equations of elasticity

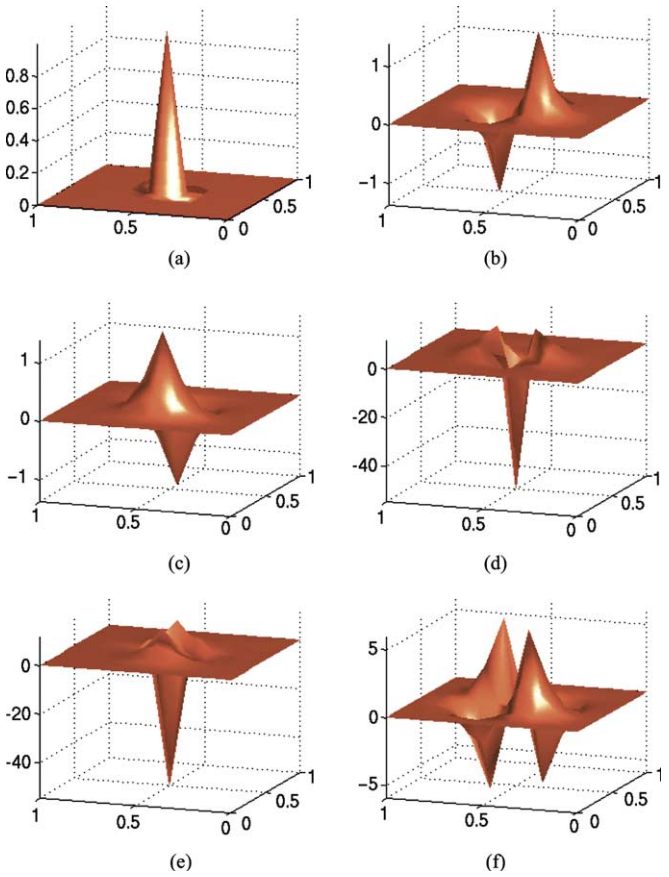

Fig. 2. 2D fixed kernel interpolation function and its derivatives: (a) $N(x,y)$, (b) $\partial N(x,y)/\partial x$, (c) $\partial N(x,y)/\partial y$, (d) $\partial^2 N(x,y)/\partial x^2$, (e) $\partial^2 N(x,y)/\partial y^2$, (f) $\partial^2 N(x,y)/\partial x \partial y$.

$$\begin{cases} \nabla^2 u + \dfrac{1}{1-2v'}\dfrac{\partial}{\partial x}\left(\dfrac{\partial u}{\partial x}+\dfrac{\partial v}{\partial y}\right) = 0, \\ \nabla^2 v + \dfrac{1}{1-2v'}\dfrac{\partial}{\partial y}\left(\dfrac{\partial u}{\partial x}+\dfrac{\partial v}{\partial y}\right) = 0, \end{cases} \tag{20}$$

with

$$v' = \begin{cases} v & \text{for plane strain,} \\ \dfrac{v}{1+v} & \text{for plane stress,} \end{cases} \tag{21}$$

where v is the Poisson's ratio. In this paper we consider plane stress situation. For an interior node, Eq. (20) is approximated by the fixed kernel interpolation given by Eqs. (15)–(19). For a node J satisfying the equilibrium equation, we obtain

$$\begin{cases} \dfrac{2}{1-v}\sum_{I=1}^{\mathrm{NP}} \dfrac{\partial^2 N_I(x_j,y_j)}{\partial x^2}\hat{\boldsymbol{u}}_I + \dfrac{1+v}{1-v}\sum_{I=1}^{\mathrm{NP}} \dfrac{\partial^2 N_I(x_j,y_j)}{\partial x \partial y}\hat{\boldsymbol{v}}_I + \sum_{I=1}^{\mathrm{NP}} \dfrac{\partial^2 N_I(x_j,y_j)}{\partial y^2}\hat{\boldsymbol{u}}_I = 0, \\ \dfrac{2}{1-v}\sum_{I=1}^{\mathrm{NP}} \dfrac{\partial^2 N_I(x_j,y_j)}{\partial y^2}\hat{\boldsymbol{v}}_I + \dfrac{1+v}{1-v}\sum_{I=1}^{\mathrm{NP}} \dfrac{\partial^2 N_I(x_j,y_j)}{\partial x \partial y}\hat{\boldsymbol{u}}_I + \sum_{I=1}^{\mathrm{NP}} \dfrac{\partial^2 N_I(x_j,y_j)}{\partial x^2}\hat{\boldsymbol{v}}_I = 0, \end{cases} \tag{22}$$

where (x_j, y_j) is the coordinate of node J, and v is the Poisson's ratio.

For a node K with a Dirichlet-type boundary condition on the x-component of the displacement (e.g. $u^a = g$), we obtain

$$\sum_{I=1}^{\mathrm{NP}} N_I(x_k, y_k)\hat{\boldsymbol{u}}_I = g, \tag{23}$$

where (x_k, y_k) refers to the location of node K.

Similarly, for a node L with a Neumann-type boundary condition (e.g. $f(u_{,x}) = h_x$ in the expressions of the tractions), we obtain

$$\sum_{I=1}^{\mathrm{NP}} f\left(\frac{\partial N_I(x_l, y_l)}{\partial x}\hat{\boldsymbol{u}}_I\right) = h_x, \tag{24}$$

where (x_l, y_l) is the coordinate of node L.

Combining Eqs. (22)–(24) for all the nodes, we obtain a linear system of equations

$$\mathbf{K}\hat{\mathbf{u}} = \mathbf{f}, \tag{25}$$

where $\mathbf{K}$, $\mathbf{f}$ are the coefficient matrix and the right hand side, respectively. The solution of Eq. (25) gives the nodal parameters $\hat{\boldsymbol{u}}_I$ and $\hat{v}_I$. Once the nodal parameters are known, the x- and y-displacements are computed by

$$u^a(x,y) = \sum_{I=1}^{\mathrm{NP}} N_I(x,y)\hat{\boldsymbol{u}}_I \qquad v^a(x,y) = \sum_{I=1}^{\mathrm{NP}} N_I(x,y)\hat{v}_I. \tag{26}$$

4. Boundary element method for 2-D elastostatics

The boundary integral equation of 2-D elastostatics is given by

$$\mathbf{C}\mathbf{u} = \int_\Gamma \mathbf{u}^*\mathbf{t}\,\mathrm{d}\Gamma - \int_\Gamma \mathbf{t}^*\mathbf{u}\,\mathrm{d}\Gamma + \int_\Omega \mathbf{u}^*\mathbf{b}\,\mathrm{d}\Omega, \tag{27}$$

where $\mathbf{C}$ is the corner tensor, $\mathbf{u}$ and $\mathbf{t}$ are the displacement and the traction vectors, respectively, $\mathbf{u}^*$ and $\mathbf{t}^*$ are the displacement and the traction fundamental solution vectors, respectively, and $\mathbf{b}$ is the body force vector, which is not considered here. According to the notation established previously, Ω denotes the domain and Γ denotes the boundary of the body. The fundamental solutions for the 2-D elastostatics are given by [10]

$$u^*_{lk} = \frac{1+\nu'}{4\pi E'(1-\nu')}\left[(3-4\nu')ln\left(\frac{1}{r}\right)\delta_{lk} + \frac{\partial r}{\partial x_l}\frac{\partial r}{\partial x_k}\right], \tag{28}$$

$$t^*_{lk} = -\frac{1}{4\pi(1-\nu')r}\left[\frac{\partial r}{\partial n}\left\{(1-2\nu')\delta_{kl} + 2\frac{\partial r}{\partial x_k}\frac{\partial r}{\partial x_l}\right\} - (1-2\nu')\left(\frac{\partial r}{\partial x_l}n_k - \frac{\partial r}{\partial x_k}n_l\right)\right], \tag{29}$$

with

$$\nu' = \nu, \quad E' = E, \text{ for plane strain} \tag{30}$$

and

$$\nu' = \frac{\nu}{1+\nu}, \quad E' = E(1-\nu'^2), \text{ for plane stress,} \tag{31}$$

where E is the Young's modulus and v is the Poisson's ratio. Moreover, r is the distance between the source and the field points, and $\mathbf{n}$ is the unit outward normal vector on the boundary.

The boundary of the domain is discretized into a set of small elements. Each element contains one or more collocation nodes. The boundary integral equations are satisfied at each collocation node. Various types of elements have been used in the literature. In this work, quadratic elements are used. Thus, the boundary integral equation can be discretized as (in the absence of body forces)

$$\mathbf{C}_i\mathbf{u}_i = \sum_{j=1}^{\mathrm{NE}} \int_{\Gamma_j} \mathbf{u}^*\mathbf{t}\,\mathrm{d}\Gamma - \sum_{j=1}^{\mathrm{NE}} \int_{\Gamma_j} \mathbf{t}^*\mathbf{u}\,\mathrm{d}\Gamma, \tag{32}$$

where i refers to the collocation point, and NE is the number of elements. Although we have selected quadratic boundary elements, any other interpolation order can be used in the coupling scheme. For quadratic elements, the displacements $\mathbf{u}$ and tractions $\mathbf{t}$ in an element are written as

$$\mathbf{u}(x,y) = [\,\Phi_1(x,y) \quad \Phi_2(x,y) \quad \Phi_3(x,y)\,] \begin{bmatrix} \mathbf{u_1} \\ \mathbf{u_2} \\ \mathbf{u_3} \end{bmatrix}, \tag{33}$$

$$\mathbf{t}(x,y) = [\,\Phi_1(x,y) \quad \Phi_2(x,y) \quad \Phi_3(x,y)\,] \begin{bmatrix} \mathbf{t_1} \\ \mathbf{t_2} \\ \mathbf{t_3} \end{bmatrix}, \tag{34}$$

where $\mathbf{u}_h$ and $\mathbf{t}_h$, $h = 1,\ldots,3$, are the displacements and the tractions on the element, and Φ_h are the quadratic interpolation functions given by

$$\Phi_1 = \frac{\xi(\xi-1)}{2}, \quad \Phi_2 = 1-\xi^2, \quad \Phi_3 = \frac{\xi(\xi+1)}{2}. \tag{35}$$

Substituting the interpolations for displacements and the tractions, Eq. (32) can be written as

$$\mathbf{C}_i\mathbf{u}_i = \sum_{j=1}^{\mathrm{NE}} \int_{\Gamma_j} \mathbf{u}^*\Phi\,\mathrm{d}\Gamma\mathbf{t}_j - \sum_{j=1}^{\mathrm{NE}} \int_{\Gamma_j} \mathbf{t}^*\Phi\,\mathrm{d}\Gamma\mathbf{u}_j. \tag{36}$$

Equation (36) gives rise to a linear system of equations

$$\mathbf{G}\mathbf{u} = \mathbf{H}\mathbf{t}, \tag{37}$$

where $\mathbf{G}$, $\mathbf{H}$ are the coefficient matrices. The solution of Eq. (37) gives the unknown nodal displacements or tractions at the nodes.

5. The BEM/FCM coupling approach

In the proposed BEM/FCM coupling approach, the physical domain is divided into BEM and FCM subdomains, as shown in Fig. 3. The boundary of the BEM region (denoted by **B**) is divided into elements, and points are sprinkled over the FCM region (denoted by **F**). The nodes at the interface (denoted by **I**) are shared by both the FCM and BEM regions. Numerical procedures are carried out for each domain by means of their corresponding method (see Sections 3 and 4). Once the final linear systems for all the subdomains are obtained, they are assembled into the coupled linear system, which includes unknowns associated with the BEM subdomain, unknowns associated with the FCM subdomains, and common unknowns at the interface between the BEM and the FCM subdomains. Thus, all the unknowns can be computed by solving the final coupled linear system.

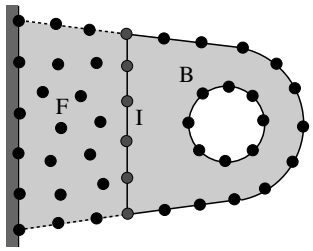

Fig. 3. Coupled FCM and BEM regions.

The final matrix form of the FCM subdomain (Eq. (25)) can be rewritten as

$$\mathbf{K}^{\mathbf{F}}\hat{\mathbf{u}}^{\mathbf{F}} = \mathbf{f} = \begin{Bmatrix} \mathbf{s}^{\mathbf{F}} \\ \mathbf{t}_{\mathbf{I}}^{\mathbf{F}} \end{Bmatrix} = [\mathbf{I}] \begin{Bmatrix} \mathbf{s}^{\mathbf{F}} \\ \mathbf{t}_{\mathbf{I}}^{\mathbf{F}} \end{Bmatrix} = [\mathbf{I}_1 \quad \mathbf{I}_2] \begin{Bmatrix} \mathbf{s}^{\mathbf{F}} \\ \mathbf{t}_{\mathbf{I}}^{\mathbf{F}} \end{Bmatrix}, \tag{38}$$

where $\mathbf{K}^{\mathbf{F}}$ is the stiffness matrix of the FCM subdomain, $\hat{\mathbf{u}}^{\mathbf{F}}$ denotes the nodal parameters, $\mathbf{s}^{\mathbf{F}}$ contains the known nodal body force, prescribed displacement or prescribed traction (not force), $\mathbf{t}_{\mathbf{I}}^{\mathbf{F}}$ is the unknown nodal traction at the interface, and $[\mathbf{I}]$ is the identity matrix. Note that, for the purpose of assembling the final coupled matrices, the right hand side of the FCM final linear system is multiplied by an identity matrix and then divided into non-interface and interface parts, $\mathbf{I}_1$ and $\mathbf{I}_2$, respectively. Similarly, The final matrix form of the BEM subdomain (Eq. (37)) can be rewritten as

$$[\mathbf{H}^{\mathbf{B}} \quad \mathbf{H}_{\mathbf{I}}^{\mathbf{B}}] \begin{Bmatrix} \mathbf{u}^{\mathbf{B}} \\ \mathbf{u}_{\mathbf{I}}^{\mathbf{B}} \end{Bmatrix} = [\mathbf{G}^{\mathbf{B}} \quad \mathbf{G}_{\mathbf{I}}^{\mathbf{B}}] \begin{Bmatrix} \mathbf{t}^{\mathbf{B}} \\ \mathbf{t}_{\mathbf{I}}^{\mathbf{B}} \end{Bmatrix}, \tag{39}$$

where $\mathbf{H}^{\mathbf{B}}$ and $\mathbf{G}^{\mathbf{B}}$ are the coefficient matrices of the BEM subdomain (see Eq. (37)), $\mathbf{u}^{\mathbf{B}}$ denotes the nodal displacements of the BEM subdomain, and $\mathbf{t}^{\mathbf{B}}$ refers to the nodal tractions of the BEM subdomain.

Applying the interface compatibility and equilibrium conditions:

$$\mathbf{u}_{\mathbf{I}} = \mathbf{u}_{\mathbf{I}}^{\mathbf{B}} = \mathbf{u}_{\mathbf{I}}^{\mathbf{F}} = \mathbf{N}\hat{\mathbf{u}}^{\mathbf{F}}, \tag{40}$$

$$\mathbf{t}_{\mathbf{I}} = \mathbf{t}_{\mathbf{I}}^{\mathbf{B}} = -\mathbf{t}_{\mathbf{I}}^{\mathbf{F}}, \tag{41}$$

respectively, where $\mathbf{N}$ is the interpolation function sub-matrix of the FCM subdomain (see Eq. (26)), we have

$$\begin{bmatrix} \mathbf{H}^{\mathbf{B}} & \mathbf{H}_{\mathbf{I}}^{\mathbf{B}}\mathbf{N} & -\mathbf{G}_{\mathbf{I}}^{\mathbf{B}} \\ \mathbf{0} & \mathbf{K}^{\mathbf{F}} & \mathbf{I}_2 \end{bmatrix} \begin{Bmatrix} \mathbf{u}^{\mathbf{B}} \\ \hat{\mathbf{u}}_{\mathbf{F}} \\ \mathbf{t}_{\mathbf{I}} \end{Bmatrix} = \begin{bmatrix} \mathbf{G}^{\mathbf{B}} & \mathbf{0} \\ \mathbf{0} & \mathbf{I}_1 \end{bmatrix} \begin{Bmatrix} \mathbf{t}^{\mathbf{B}} \\ \mathbf{s}^{\mathbf{F}} \end{Bmatrix}. \tag{42}$$

The linear system above is rearranged according to the boundary conditions. The final coupled linear system is typically not symmetric since the blocks of FCM and BEM in Eq. (42) are all non-symmetric. However, it can be conveniently solved by means of sparse solvers [29]. Notice that the BEM blocks are fully populated, and the FCM blocks are sparse. After the unknown $\hat{\mathbf{u}}_{\mathbf{F}}$ is computed, the nodal displacements $\mathbf{u}^{\mathbf{F}}$ in the FCM subdomain can be computed by using Eq. (26).

The FCM/BEM coupling approach can be easily extended to solve multizone problems where a physical domain is divided into various multi-subdomains. An example, is given in Fig. 4, where the domain has three regions with different material properties [30]. Therefore, the regions need to be treated separately. Assume that the domain is divided into 1 FCM region and 2 BEM regions as shown in Fig. 4. The FCM subdomain is denoted as F_1, and the BEM subdomains are denoted as B_1 and B_2. The interface F_1B_1 refers to the interface of the subdomain F_1 and the subdomain B_1. The other interfaces are defined similarly. Note that the corner point C is shared by the three regions F_1, B_1 and B_2.

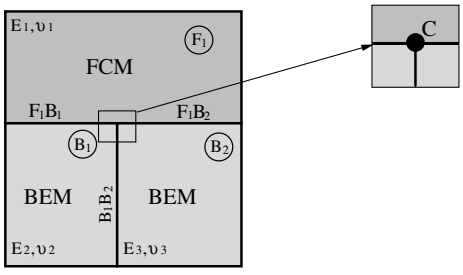

Fig. 4. A multizone problem.

The final matrix form of the FCM region can be written as

$$\mathbf{K}^{\mathbf{F}_1}\hat{\mathbf{u}}^{\mathbf{F}_1} = \begin{bmatrix} \mathbf{I}_1^{\mathbf{F}_1} & \mathbf{I}_2^{\mathbf{F}_1} & \mathbf{I}_3^{\mathbf{F}_1} & \mathbf{I}_4^{\mathbf{F}_1} \end{bmatrix} \begin{Bmatrix} \mathbf{s}^{\mathbf{F}_1} \\ \mathbf{t}_{\mathbf{F}_1\mathbf{B}_1}^{\mathbf{F}_1} \\ \mathbf{t}_{\mathbf{F}_1\mathbf{B}_2}^{\mathbf{F}_1} \\ \mathbf{t}_{\mathbf{C}}^{\mathbf{F}_1} \end{Bmatrix}. \tag{43}$$

The final matrix form of the two BEM regions (B_1 and B_2) can be written as

$$\begin{bmatrix} \mathbf{H}^{\mathbf{B}_1} & \mathbf{H}_{\mathbf{F}_1\mathbf{B}_1}^{\mathbf{B}_1} & \mathbf{H}_{\mathbf{B}_1\mathbf{B}_2}^{\mathbf{B}_1} \end{bmatrix} \begin{Bmatrix} \mathbf{u}^{\mathbf{B}_1} \\ \mathbf{u}_{\mathbf{F}_1\mathbf{B}_1}^{\mathbf{B}_1} \\ \mathbf{u}_{\mathbf{B}_1\mathbf{B}_2}^{\mathbf{B}_1} \end{Bmatrix} = \begin{bmatrix} \mathbf{G}^{\mathbf{B}_1} & \mathbf{G}_{\mathbf{F}_1\mathbf{B}_1}^{\mathbf{B}_1} & \mathbf{G}_{\mathbf{B}_1\mathbf{B}_2}^{\mathbf{B}_1} & \mathbf{G}_{\mathbf{C}}^{\mathbf{B}_1} \end{bmatrix} \begin{Bmatrix} \mathbf{t}^{\mathbf{B}_1} \\ \mathbf{t}_{\mathbf{F}_1\mathbf{B}_1}^{\mathbf{B}_1} \\ \mathbf{t}_{\mathbf{B}_1\mathbf{B}_2}^{\mathbf{B}_1} \\ \mathbf{t}_{\mathbf{C}}^{\mathbf{B}_1} \end{Bmatrix}, \tag{44}$$

$$\begin{bmatrix} \mathbf{H}^{\mathbf{B}_2} & \mathbf{H}_{\mathbf{F}_1\mathbf{B}_2}^{\mathbf{B}_2} & \mathbf{H}_{\mathbf{B}_1\mathbf{B}_2}^{\mathbf{B}_2} \end{bmatrix} \begin{Bmatrix} \mathbf{u}^{\mathbf{B}_2} \\ \mathbf{u}_{\mathbf{F}_1\mathbf{B}_2}^{\mathbf{B}_2} \\ \mathbf{u}_{\mathbf{B}_1\mathbf{B}_2}^{\mathbf{B}_2} \end{Bmatrix} = \begin{bmatrix} \mathbf{G}^{\mathbf{B}_2} & \mathbf{G}_{\mathbf{F}_1\mathbf{B}_2}^{\mathbf{B}_2} & \mathbf{G}_{\mathbf{B}_1\mathbf{B}_2}^{\mathbf{B}_2} & \mathbf{G}_{\mathbf{C}}^{\mathbf{B}_2} \end{bmatrix} \begin{Bmatrix} \mathbf{t}^{\mathbf{B}_2} \\ \mathbf{t}_{\mathbf{F}_1\mathbf{B}_2}^{\mathbf{B}_2} \\ \mathbf{t}_{\mathbf{B}_1\mathbf{B}_2}^{\mathbf{B}_2} \\ \mathbf{t}_{\mathbf{C}}^{\mathbf{B}_2} \end{Bmatrix}, \tag{45}$$

respectively. The interface compatibility conditions for this example are

$$\begin{cases} \mathbf{u}_{\mathbf{F}_1\mathbf{B}_1} = \mathbf{u}_{\mathbf{F}_1\mathbf{B}_1}^{\mathbf{F}_1} = \mathbf{u}_{\mathbf{F}_1\mathbf{B}_1}^{\mathbf{B}_1} \\ \mathbf{u}_{\mathbf{F}_1\mathbf{B}_2} = \mathbf{u}_{\mathbf{F}_1\mathbf{B}_2}^{\mathbf{F}_1} = \mathbf{u}_{\mathbf{F}_1\mathbf{B}_2}^{\mathbf{B}_2} \\ \mathbf{u}_{\mathbf{B}_1\mathbf{B}_2} = \mathbf{u}_{\mathbf{B}_1\mathbf{B}_2}^{\mathbf{B}_1} = \mathbf{u}_{\mathbf{B}_1\mathbf{B}_2}^{\mathbf{B}_2} \end{cases} \quad \begin{cases} \mathbf{t}_{\mathbf{F}_1\mathbf{B}_1} = \mathbf{t}_{\mathbf{F}_1\mathbf{B}_1}^{\mathbf{F}_1} = -\mathbf{t}_{\mathbf{F}_1\mathbf{B}_1}^{\mathbf{B}_1}, \\ \mathbf{t}_{\mathbf{F}_1\mathbf{B}_2} = \mathbf{t}_{\mathbf{F}_1\mathbf{B}_2}^{\mathbf{F}_1} = -\mathbf{t}_{\mathbf{F}_1\mathbf{B}_2}^{\mathbf{B}_2}, \\ \mathbf{t}_{\mathbf{B}_1\mathbf{B}_2} = \mathbf{t}_{\mathbf{B}_1\mathbf{B}_2}^{\mathbf{B}_1} = -\mathbf{t}_{\mathbf{B}_1\mathbf{B}_2}^{\mathbf{B}_2}, \\ \mathbf{t}_{\mathbf{C}}^{\mathbf{F}_1} + \mathbf{t}_{\mathbf{C}}^{\mathbf{B}_1} + \mathbf{t}_{\mathbf{C}}^{\mathbf{B}_2} = \mathbf{0}. \end{cases} \tag{46}$$

Applying the compatibility conditions, the coupled multizone linear system can be assembled as

$$\begin{bmatrix} \mathbf{K}^{\mathbf{F}_1} & \mathbf{0} & \mathbf{0} & \mathbf{0} & -\mathbf{I}_2^{\mathbf{F}_1} & -\mathbf{I}_3^{\mathbf{F}_1} & \mathbf{0} & \mathbf{I}_4^{\mathbf{F}_1} & \mathbf{I}_4^{\mathbf{F}_1} \\ \mathbf{H}_{\mathbf{F}_1\mathbf{B}_1}^{\mathbf{B}_1}\mathbf{N}_{\mathbf{F}_1\mathbf{B}_1} & \mathbf{H}^{\mathbf{B}_1} & \mathbf{0} & \mathbf{H}_{\mathbf{B}_1\mathbf{B}_2}^{\mathbf{B}_1} & \mathbf{G}_{\mathbf{F}_1\mathbf{B}_1}^{\mathbf{B}_1} & \mathbf{0} & -\mathbf{G}_{\mathbf{B}_1\mathbf{B}_2}^{\mathbf{B}_1} & -\mathbf{G}_{\mathbf{C}}^{\mathbf{B}_1} & \mathbf{0} \\ \mathbf{H}_{\mathbf{F}_1\mathbf{B}_2}^{\mathbf{B}_2}\mathbf{N}_{\mathbf{F}_1\mathbf{B}_2} & \mathbf{0} & \mathbf{H}^{\mathbf{B}_2} & \mathbf{H}_{\mathbf{B}_1\mathbf{B}_2}^{\mathbf{B}_2} & \mathbf{0} & \mathbf{G}_{\mathbf{F}_1\mathbf{B}_2}^{\mathbf{B}_2} & \mathbf{G}_{\mathbf{B}_1\mathbf{B}_2}^{\mathbf{B}_2} & \mathbf{0} & -\mathbf{G}_{\mathbf{C}}^{\mathbf{B}_2} \end{bmatrix} \begin{Bmatrix} \hat{\mathbf{u}}^{\mathbf{F}_1} \\ \mathbf{u}^{\mathbf{B}_1} \\ \mathbf{u}^{\mathbf{B}_2} \\ \mathbf{u}_{\mathbf{B}_1\mathbf{B}_2} \\ \mathbf{t}_{\mathbf{F}_1\mathbf{B}_1} \\ \mathbf{t}_{\mathbf{F}_1\mathbf{B}_2} \\ \mathbf{t}_{\mathbf{B}_1\mathbf{B}_2} \\ \mathbf{t}_{\mathbf{C}}^{\mathbf{B}_1} \\ \mathbf{t}_{\mathbf{C}}^{\mathbf{B}_2} \end{Bmatrix}$$

$$= \begin{bmatrix} \mathbf{I}_1^{\mathbf{F}_1} & \mathbf{0} & \mathbf{0} \\ \mathbf{0} & \mathbf{G}^{\mathbf{B}_1} & \mathbf{0} \\ \mathbf{0} & \mathbf{0} & \mathbf{G}^{\mathbf{B}_2} \end{bmatrix} \begin{Bmatrix} \mathbf{s}^{\mathbf{F}_1} \\ \mathbf{t}^{\mathbf{B}_1} \\ \mathbf{t}^{\mathbf{B}_2} \end{Bmatrix}, \tag{47}$$

where $\mathbf{N}_{\mathbf{F_1B_1}}$ and $\mathbf{N}_{\mathbf{F_1B_2}}$ is the FCM interpolation sub-matrix for the shared points at the interfaces F_1B_1 and F_1B_2, respectively. This is the final linear system which can be solved for the various unknowns in the problem.

6. Numerical results

Three examples of 2-D elastostatic analysis are given in this section and presented in order of increasing complexity:

1. Patch test
2. Cantilever beam
3. Plate with holes

In all the examples, normalized and consistent physical units are employed. The convergence of the FCM/BEM coupling approach is measured by using a global error measure [2]

$$\varepsilon = \frac{1}{|u^{(e)}|_{\max}} \sqrt{\frac{1}{NT} \sum_{I=1}^{NT} [u_I^{(e)} - u_I^{(c)}]^2}, \tag{48}$$

where ε is the error in the solution, NT is the total number of nodes (or points), and the superscripts (e) and (c) denote, respectively, the exact and the computed solutions.

6.1. Patch test

The first example is the plane stress patch test as shown in Fig. 5. In this example, a unit surface traction is applied at the right side of a 2×1 plate. The FCM and BEM regions are shown in Fig. 5(a) and the computed deformation is shown in Fig. 5(b). The Young's modulus of 1.0 and the Poisson's ratio of 0.25 are used in this example. The exact solution is given by

$$u = x, \quad v = -\frac{y}{4}. \tag{49}$$

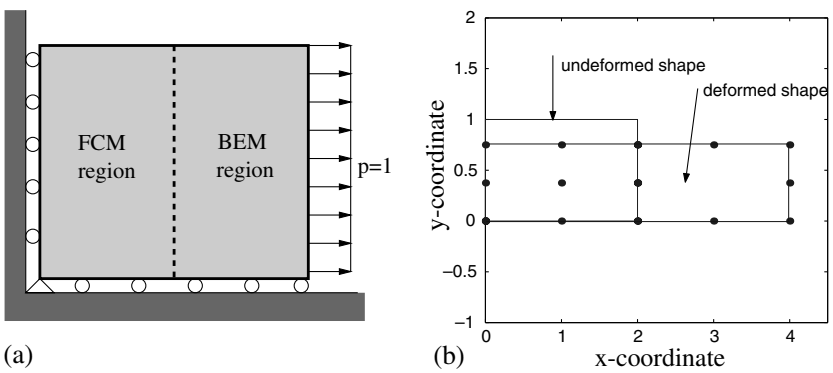

Fig. 5. (a) Patch test, (b) computed result using nine FCM points and four BEM elements (coarse discretization).

Table 1
Patch test: comparison of computed displacements at $(x, y) = (2, 0.5)$ with the exact solution and properties of the problem

Discretization	# of DOFs	Condition number	$u(2, 0.5)$	$v(2, 0.5)$
9 FCM points and 4 BEM elements	34	281	1.999768	−0.125092
25 FCM points and 8 BEM elements	82	1.5×10^3	2.000083	−0.124962
81 FCM points and 16 BEM elements	226	1.3×10^4	2.000016	−0.124982
289 FCM points and 32 BEM elements	706	1.1×10^5	2.000008	−0.124994
Exact solution	–	–	2.0	−0.125

Different point/element discretizations are applied to solve the problem. Table 1 shows a comparison of the computed results and the exact solution at the point $(x, y) = (2, 0.5)$. Excellent results are obtained and the convergence rates of the coupling approach for this example are 1.2 for u displacement, and 1.23 for v displacement (see Fig. 6). Table 1 also provides the number of degrees of freedom (DOFs) and the condition number for the various coupled system. Note that while reasonably well-conditioned matrices are obtained, the condition number of the final matrix is approximately a quadratic function of DOFs of the problem. To illustrate the matrix sparsity pattern obtained with the present coupling strategy, the image of the final coefficient matrix for the last case of Table 1 is shown in Fig. 7. Notice that the total matrix size is 706×706 or 498,436 entries. However, only 46,925 entries are nonzero, i.e. 9.4%.

6.2. Cantilever beam

The second example is a cantilever beam subjected to a shear force, as shown in Fig. 8. The material properties are identical to those of the first example. The exact solution is given by [28]:

$$u = -\frac{P}{6EI}\left(y - \frac{D}{2}\right)[3x(2L - x) + (2 + v)y(y - D)], \tag{50}$$

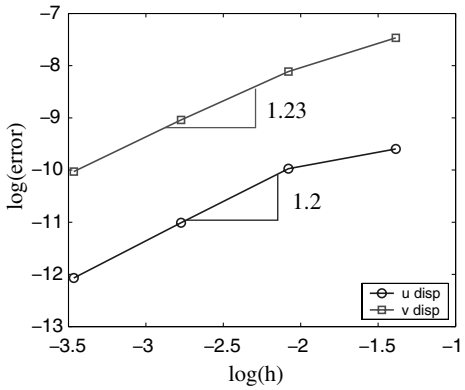

Fig. 6. Convergence plot of the displacements.

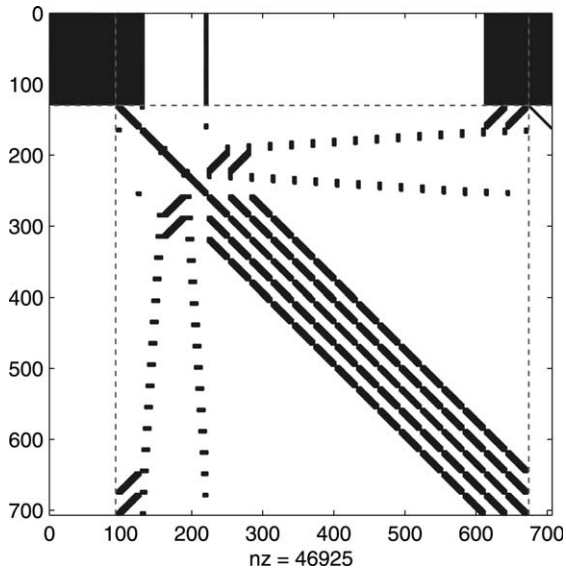

Fig. 7. Image of the final coefficient matrix of Eq. (42). The sizes of the block matrices are the following: $\mathbf{H}^{\mathbf{B}}$: 128×96; $\mathbf{H}_{\mathbf{I}}^{\mathbf{B}}\mathbf{N}$: 128×578; $\mathbf{G}_{\mathbf{I}}^{\mathbf{B}}$: 128×32; $\mathbf{0}$: 578×96; $\mathbf{K}^{\mathbf{F}}$: 578×578; $\mathbf{I}_2$: 578×32.

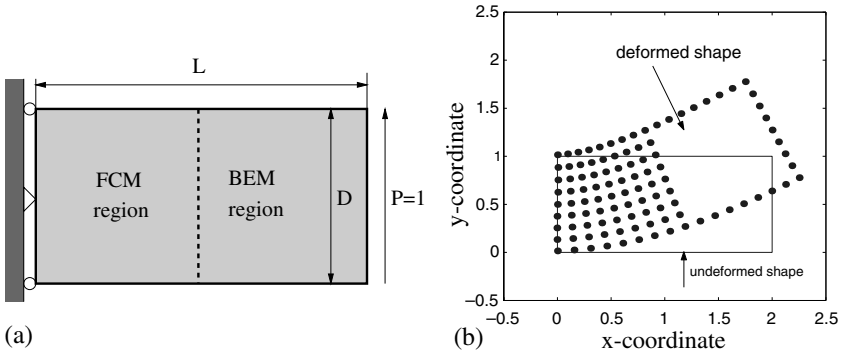

Fig. 8. (a) Cantilever beam, (b) computed result using 81 FCM points and 16 BEM elements.

$$v = \frac{P}{6EI}\left[x^2(3L - x) + 3v(L - x)\left(y - \frac{D}{2}\right)^2 + \frac{4 + 5v}{4}D^2x\right], \tag{51}$$

where P is the shear force, L and D are the length and the height of the beam, respectively, and I is the moment of inertia. In this example, $L = 2$, $D = 1$, thickness $= 1$, and the cross-section is rectangular. The FCM and BEM regions are shown in Fig. 8(a) and the computed deformation is shown in Fig. 8(b). Table 2 shows a comparison of the computed displacement at the point $(x, y) = (2, 1)$ with the exact solution. The results converge monotonically to the exact solution and the convergence rates are found to be 2.25 for u displacement and 2.5 for v displacement (Fig. 9). Table 2 also provides the number of DOFs and the

Table 2
Cantilever beam: comparison of computed displacements at $(x, y) = (2, 1)$ with the exact solution and properties of the problem

Discretization	# of DOFs	Condition number	$u(2,1)$	$v(2,1)$
25 FCM points and 8 BEM elements	82	3.5×10^4	−0.279602	0.862080
81 FCM points and 16 BEM elements	226	8.7×10^4	−0.250112	0.776138
289 FCM points and 32 BEM elements	706	6.5×10^5	−0.241930	0.751646
1089 FCM points and 64 BEM elements	2434	6.2×10^6	−0.239858	0.745168
Exact solution	–	–	−0.24	0.745

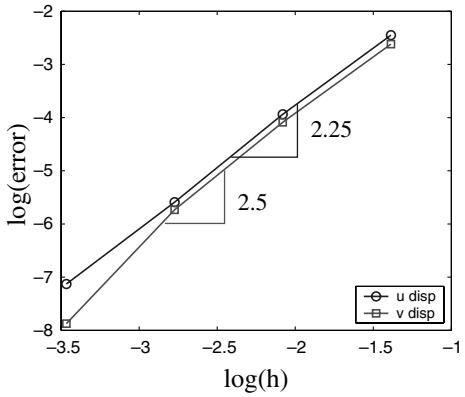

Fig. 9. Convergence plot of the displacements.

condition number for the system matrix of the coupled systems, which again indicate that reasonably well-conditioned matrices are obtained.

6.3. Plate with holes

The final example deals with a more complicated problem. As shown in Fig. 10, a plate containing three holes and a notch is subjected to a uniform pressure at its right edge [31]. The problem is solved by using four methods: FEM, BEM, FCM, and FCM/BEM coupling. Furthermore, to assess the influence of interface length and shape in the FCM/BEM coupling approach, we have used three different types of interfaces. The solutions obtained from the four methods are compared in terms of accuracy, computational cost and numerical properties. We construct the BEM and FCM discretizations by employing the same set of FEM nodes. For example, as shown in Fig. 11, the FEM domain contains 25 nodes. Thus the 16 boundary FEM nodes are used as the BEM nodes, and all the 25 FEM nodes are used as the FCM points. Fig. 12(a) shows the deformed shape obtained by the FEM code ANSYS. The FEM mesh consists of 4474 nodes. Following the strategy of Fig. 11 for the example of Fig. 10, the 636 boundary nodes of the ANSYS FEM mesh are taken as the boundary nodes in BEM simulation, and all the 4474 ANSYS nodes are taken as the points in the FCM simulation. The deformed shapes obtained by BEM and FCM are shown in Fig. 12(b) and (c), respectively. For FCM/BEM coupling, the domain is divided into FCM and BEM regions by using three types of interfaces: straight line, semi-circular and wave shaped. The deformed shapes for the three cases are shown in Fig. 13(a), (b) and (c), respectively. The results obtained from all the approaches agree with each other quite well and the difference of the maximum displacement is within 1%. Fig. 14 shows the σ_{xx} stress distribution obtained from the FCM/BEM coupling approach with a wave-shaped

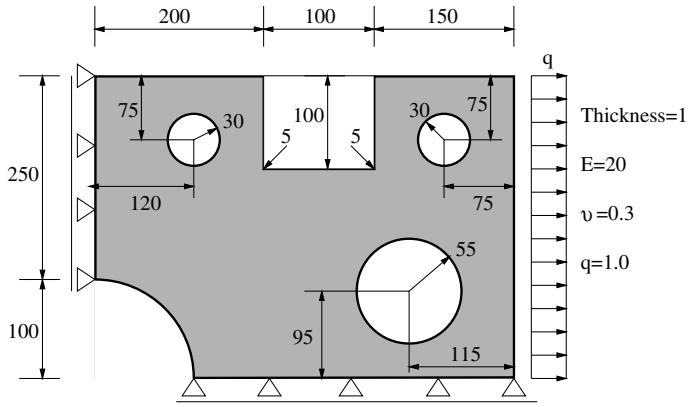

Fig. 10. Plate with holes.

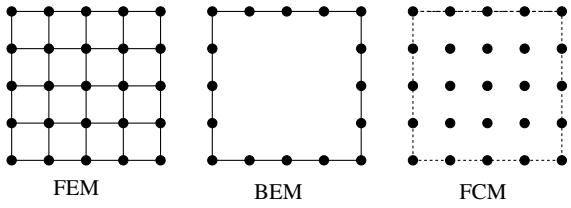

Fig. 11. Illustration of modeling strategy for the last example.

interface. It matches quite well with previous solutions (e.g. FEM). Fig. 15 shows a quantitative comparison of the computed σ_{xx} stress on the surfaces of the holes obtained from the four methods and three interfaces. Since BEM usually gives accurate boundary stress solutions, the BEM solution is taken as the reference solution to obtain the absolute deviations of the various solutions as shown in Fig. 15. The errors for FEM, FCM and three coupling solutions (FCM/BEM 1, FCM/BEM 2, FCM/BEM 3) measured by Eq. (48) are 0.0182, 0.0030, 0.0079, 0.0040 and 0.0026, respectively. The results show very good agreement and demonstrate that the FCM/BEM coupling approach provides accurate results for problems with complex geometries. Moreover, the approach is robust for various kind of interfaces. Table 3 summarizes the numerical properties of the four methods for this example. The BEM largely reduces the DOF of the problem, however, due to the final unsymmetric dense matrix, the computational cost by using an LU solver is even larger than that of FEM. Note (although it is not a topic of this paper) that the computational cost of BEM can be largely reduced by using fast solvers such as the fast multipole method (FMM) [32,33]. The computational cost of FCM and FEM is similar in this example. Note that the computational cost of FEM includes the meshing time. Although there is no meshing process in FCM, the interpolation functions need to be computed for each node. However, the CPU time of computing interpolation functions scales linearly with respect to the number of nodes no matter the problem dimensionality (2-D or 3-D) and the complexity of the geometry, while FEM meshing time largely depends on the dimensionality and complexity of the geometry of the problem domain. The computational cost of the FCM/BEM coupling approach depends on the number of DOFs of the problem. Notice that the case with a semi-circular interface requires a lower solution time because it has much less DOFs than the other two cases (cf. Table 3). The final coupled matrix is sparse, but with relatively larger dense blocks (see, for example, the illustration in Fig. 7). For this reason, the computational cost of solving the final coupled linear system is typically higher than solving the FEM or

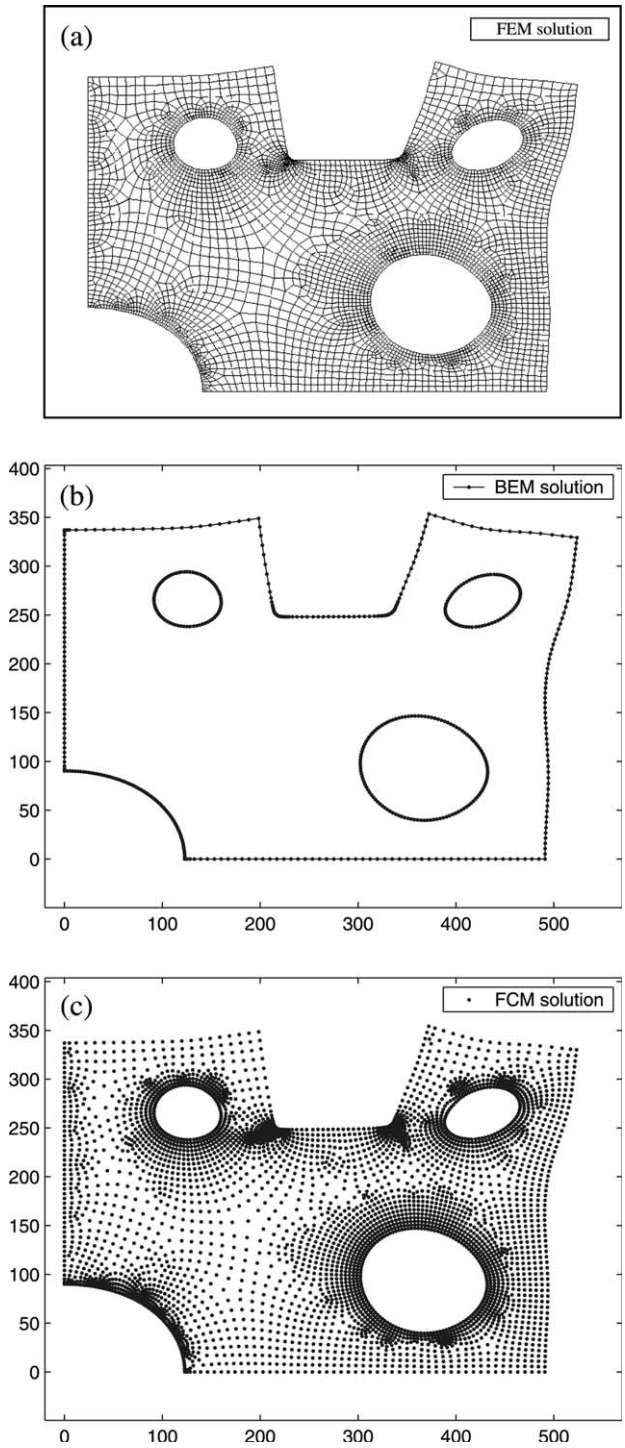

Fig. 12. Deformation of the plate: (a) FEM solution, (b) BEM solution and (c) FCM solution.

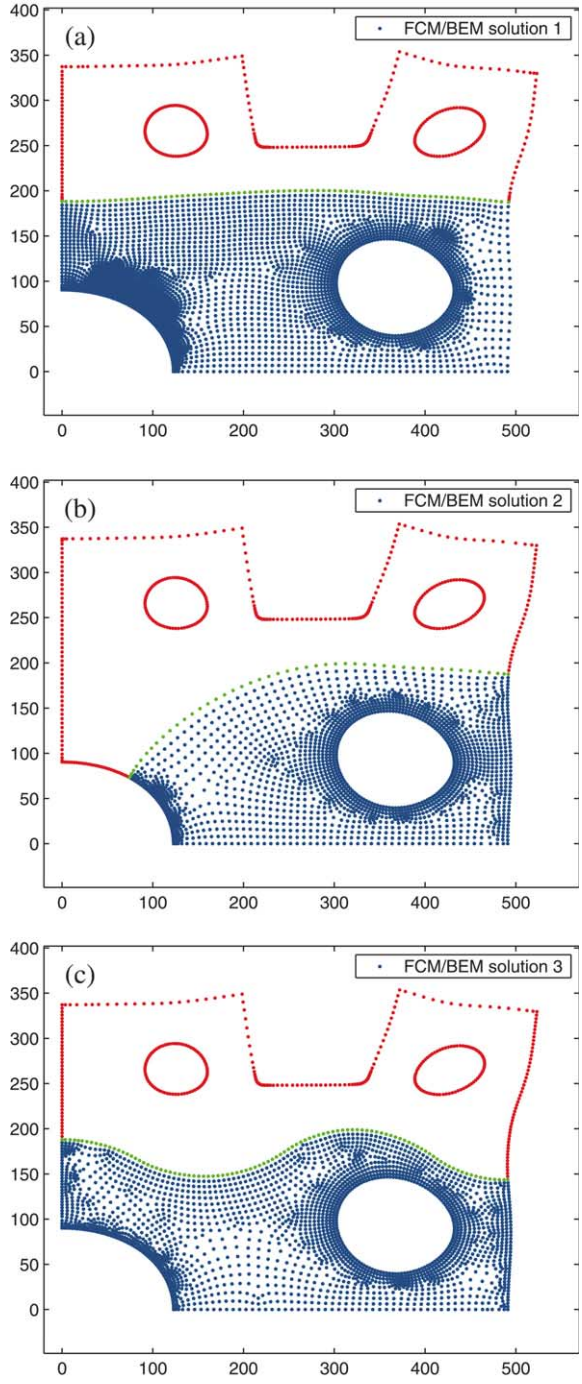

Fig. 13. Deformation of the plate with FCM/BEM coupling: (a) straight line interface, (b) semi-circular interface and (c) wave-shaped interface.

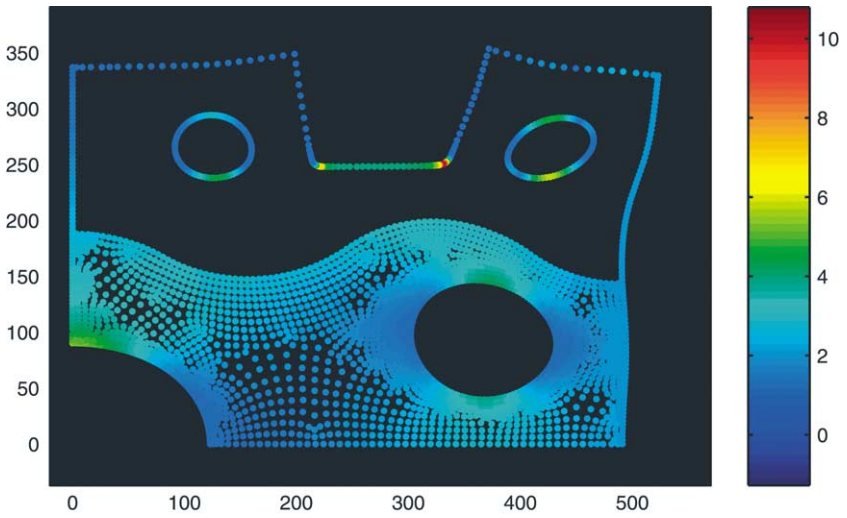

Fig. 14. The σ_{xx} distribution for the plate obtained from the FCM/BEM coupling.

FCM sparse linear system with same number of DOFs. In addition, the CPU comparisons should be understood in the context that FEM (ANSYS) used a different solver while FCM and FCM/BEM used the same sparse solver.

7. Concluding remarks and extensions

We propose a novel coupling approach for the mesh-based BEM with the meshless FCM. Compared to the conventional BEM/FEM coupling approach, the present approach offers several advantages which are discussed below.

- The FCM does not require any kind of mesh or background cells—it is a true meshless method. Thus the FCM point distribution is completely independent of the discretization of the BEM subdomain. Interior domain meshing, which could be quite difficult and expensive for complicated geometries, is completely eliminated by the present approach.
- Interface FCM points can be located at the same positions as the boundary element nodes. There is no requirement of any interpolation between the two subdomains. When the boundary elements are refined, the shared interface points of the FCM subdomain increase according to the BEM subdomain discretization.
- The coupling scheme is not restricted by the order of the boundary elements used. Therefore this feature offers greater flexibility for FCM/BEM coupling than for usual FEM/BEM coupling.
- Inherently the FCM has traction–displacement relations which are the same as those for BEM formulations, and thus no force-to-traction or traction-to-force transformations are needed in the FCM/BEM coupling scheme.

The range of application of the idea of coupling a mesh-based boundary method (BEM) with a meshless-based domain method (FCM) is quite broad, although, in this paper, we have concentrated only on linear elastostatics. Potential extensions of this work includes the solution of problems in other areas

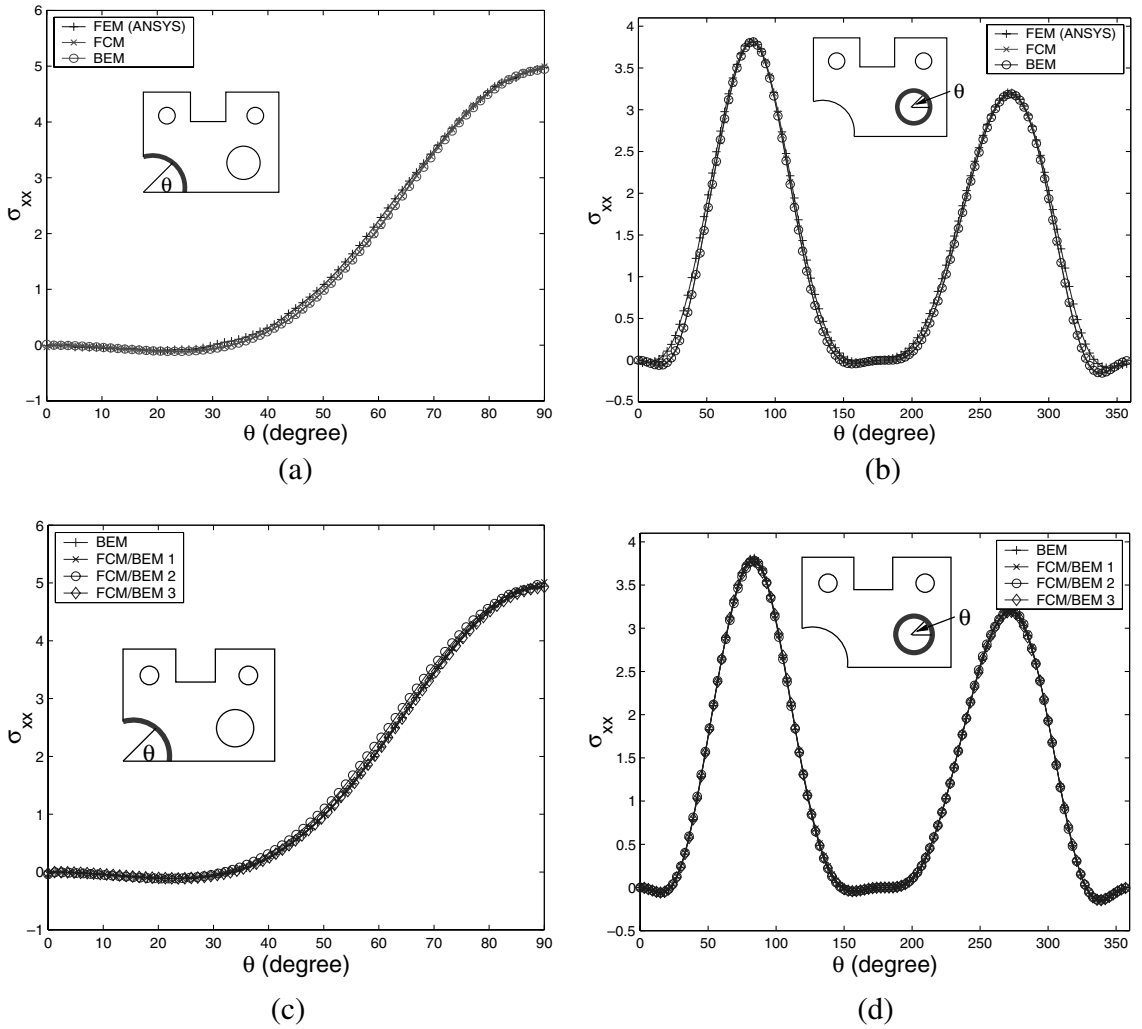

Fig. 15. Comparison of σ_{xx} at the surfaces of the holes: (a) FEM, BEM and FCM solutions for the hole centered at (0,0); (b) FEM, BEM and FCM solutions for the hole centered at (335,95); (c) FCM/BEM coupling with straight line, semi-circular and wave-shaped interfaces compared with BEM solution for the hole centered at (0,0); (d) FCM/BEM coupling with straight line, semi-circular and wave-shaped interfaces compared with BEM solution for the hole centered at (335,95).

Table 3
Comparison of numerical properties of the four methods

Method	# of DOFs	Computing time (s)	Symmetry
FEM	8948	25 (meshing) + 10 (solution)	Y
BEM	1272	61	N
FCM	8948	38	N
FCM/BEM (case 1)	7780	79	N
FCM/BEM (case 2)	4800	36	N
FCM/BEM (case 3)	5660	60	N

(e.g. fracture, potential theory, electromagnetics, etc.), and development of error estimates and adaptive mesh refinement strategies for the coupled FCM/BEM.

Acknowledgements

We thank Prof. Michael Heath for his encouragement for the creation of a new boundary element class in the college of engineering, from which this work was originated. We also gratefully acknowledge the support from the Computational Science and Engineering (CSE) Program at the University of Illinois at Urbana-Champaign (UIUC).

References

[1] T. Belytschko, Y. Krongauz, D. Organ, M. Fleming, P. Krysl, Meshless methods: An overview and recent developments, Comput. Methods Appl. Mech. Engrg. 139 (1996) 3–47.
[2] N.R. Aluru, G. Li, Finite cloud method: a true meshless technique based on a fixed reproducing kernel approximation, Int. J. Numer. Methods Engrg. 50 (2001) 2373–2410.
[3] T. Belytschko, D. Organ, Y. Krongauz, A coupled finite element–element-free Galerkin method, Computat. Mech. 17 (1995) 186–195.
[4] Y. Krongauz, T. Belytschko, Enforcement of essential boundary conditions in meshless approximations using finite elements, Comput. Methods Appl. Mech. Engrg. 131 (1996) 133–145.
[5] D. Hegen, Element-free Galerkin methods in combination with finite element approaches, Comput. Methods Appl. Mech. Engrg. 135 (1995) 143–166.
[6] A. Huerta, S. Fernández-Méndez, Enrichment and coupling of the finite element and meshless methods, Int. J. Numer. Methods Engrg. 48 (2000) 1615–1636.
[7] W.K. Liu, R.A. Uras, Y. Chen, Enrichment of the finite element method with the reproducing kernel particle method, J. Appl. Mech.—Trans. ASME 64 (1997) 861–870.
[8] O.C. Zienkiewicz, D.W. Kelly, P. Bettess, Marriage a la mode—the best of both worlds (finite elements and boundary integrals), in: R. Glowinski, E.Y. Rodin, O.C. Zienkiewicz (Eds.), Energy Methods in Finite Element Analysis, Wiley, London, 1979, pp. 82–107.
[9] C.A. Brebbia, J. Dominguez, Boundary Elements An Introductory Course, McGraw-Hill, 1989.
[10] A.A. Becker, The Boundary Element Method in Engineering—A Complete Course, McGraw-Hill, 1992.
[11] P.K. Banerjee, The Boundary Element Methods in Engineering, McGraw-Hill, 1994.
[12] H. Li, G. Han, H.A. Mang, P. Torzicky, A new method for the coupling of finite element and boundary element discretized subdomains of elastic bodies, Comput. Methods Appl. Mech. Engrg. 54 (1986) 161–185.
[13] M. Yazdchi, N. Khalili, S. Valliappan, Dynamic soil–structure interaction analysis via coupled finite-element-boundary-element method, Soil Dyn. Earthquake Engrg. 18 (1999) 499–517.
[14] X. Zeng, J. Bielak, Stable symmetric finite element-boundary integral coupling methods for fluid-structure interface problems, Engrg. Anal. Boundary Elem. 15 (1995) 79–91.
[15] C. Oysu, R.T. Fenner, Two-dimensional elastic contact analysis by coupling finite element and boundary element methods, J. Strain Anal. Engrg. Des. 33 (1998) 459–468.
[16] S.P. Song, B.Q. Li, Coupled boundary/finite element method for the computation of magnetically and electrostatically levitated droplet shapes, Int. J. Numer. Methods Engrg. 44 (1999) 1055–1077.
[17] M. Kuhn, O. Steinbach, Symmetric coupling of finite and boundary elements for exterior magnetic field problems, Math. Methods Appl. Sci. 25 (2002) 357–371.
[18] T. Belytschko, Y.Y. Lu, A variational coupled FE-BE method for transient problems, Int. J. Numer. Methods Engrg. 37 (1994) 91–105.
[19] G. Yu, W.J. Mansur, J.A.M. Carrer, S.T. Lie, A more stable scheme for BEM/FEM coupling applied to two-dimensional elastodynamics, Comput. Struct. 79 (2001) 811–823.
[20] A. Pullan, High-order coupled finite element/boundary element torso model, Engrg. Anal. Boundary Elem. 43 (1996) 292–298.
[21] X. Zeng, L.F. Kallivokas, J. Bielak, A symmetric variational finite element-boundary integral equation coupling method, Comput. Struct. 46 (1993) 995–1000.
[22] S. Holzer, On the engineering analysis of 2D problems by the symmetric Galerkin boundary element method and coupled BEM/FEM, in: J.H. Kane, G. Maier, N. Tosaka, S.N. Atluri (Eds.), Advances in Boundary Element Techniques, Springer-Verlag, 1993, pp. 187–208 (Chapter 10).

[23] S. Sirtori, S. Miccoli, E. Korach, Symmetric coupling of finite elements and boundary elements, in: J.H. Kane, G. Maier, N. Tosaka, S.N. Atluri (Eds.), Advances in Boundary Element Techniques, Springer-Verlag, 1993, pp. 407–427 (Chapter 20).
[24] C. Carstensen, P. Wriggers, On the symmetric boundary element method and the symmetric coupling of boundary elements and finite elements, IMA J. Numer. Anal. 17 (1997) 201–238.
[25] L.E. Malvern, Introduction to the Mechanics of Continuum Medium, Prentice-Hall, Englewood Cliffs, NJ, 1969.
[26] X. Jin, G. Li, N.R. Aluru, On the equivalence between least-squares and kernel approximation in meshless methods, CMES: Comput. Modeling Engrg. Sci. 2 (2001) 447–462.
[27] N.R. Aluru, A point collocation method based on reproducing kernel approximations, Int. J. Numer. Methods Engrg. 47 (2000) 1083–1121.
[28] S.P. Timoshenko, J.N. Goodier, Theory of Elasticity, McGraw-Hill, 1982.
[29] M.T. Heath, Scientific Computing: An Introductory Survey, McGraw-Hill, 1997.
[30] L.J. Gray, G.H. Paulino, Symmetric Galerkin boundary integral formulation for interface and multi-zone problems, Int. J. Numer. Methods Engrg. 40 (1997) 3085–3101.
[31] G.H. Paulino, I.F.M. Menezes, J.B. Cavalcante Neto, L.F. Martha, A methodology for adaptive finite element analysis: Towards an integrated computational environment, Computat. Mech. 23 (1999) 361–388.
[32] L. Greengard, V. Rokhlin, A fast algorithm for particle simulation, J. Computat. Phys. 73 (1989) 325–348.
[33] J.D. Richardson, L.J. Gray, T. Kaplan, J.A.L. Napier, Regularized spectral multipole BEM for plane elasticity, Engrg. Anal. Boundary Elem. 25 (2001) 295–311.